CHAPTER 6

Location and sizes of forsterite grains in protoplanetary disks. Interpretation from the Herschel DIGIT programme

K. M. Maaskant, B.L. de Vries, M. Min, L.B.F.M. Waters, C. Dominik, F. Molster, A.G.G.M. Tielens

Astronomy & Astrophysics, in press (2014)

Abstract

The spectra of protoplanetary disks contain mid- and far- infrared emission features produced by forsterite dust grains. The spectral features contain information about the forsterite temperature, chemical composition and grain size. We aim to characterize how the 23 and 69 μm features can be used to constrain the physical locations of forsterite in disks. We check for consistency between two independent forsterite temperature measurements: the I_{23}/I_{69} feature strength ratio and the shape of the 69 μm band. We perform radiative transfer modeling to study the effect of disk properties to the forsterite spectral features. Temperature dependent forsterite opacities are considered in self consistent models to compute forsterite emission from protoplanetary disks. Modeling grids are presented to study the effects of grain size, disk gaps, radial mixing and optical depth to the forsterite features. Independent temperature estimates derived from the I_{23}/I_{69} feature strength ratio and the 69 μm band shape are most inconsistent for HD 141569 and Oph IRS 48. A case study of the disk of HD 141569 shows two solutions to fit the forsterite spectrum. A model with T $\sim$ 40 K, iron rich ($\sim 0-1$ % Fe) and 1 μm forsterite grains, and a model with warmer (T $\sim$ 100 K), iron free, and larger (10 μm) grains. We find that for disks with low upper limits of the 69 μm feature (most notably in flat, self-shadowed disks), the forsterite must be hot, and thus close to the star. We find no correlation between disk gaps and the

presence or absence of forsterite features. We argue that the 69 μm feature of the evolved transitional disks HD 141569 and Oph IRS 48 is most likely a tracer of larger (i.e. $\gtrsim$ 10 μm) forsterite grains.

6.1 Introduction

Protoplanetary disks are thought to be the precursors of planetary systems. Disk evolution is therefore of great importance to understand how planets are being formed (e.g. Testi et al. 2014). Through analysis of the dust emission features at infrared (IR) wavelengths, both the chemical composition of dust and the size of grains can be constrained (e.g. Henning 2010). The characterisation of the dust provides evidence of physical and chemical processes in the disk.

Silicate dust undergoes significant processing in protoplanetary disks. Whereas dust in the interstellar medium (ISM) is largely amorphous (Kemper et al., 2004), i.e., characterized by a disordered network of silicates, enriched with O, Fe, and Mg, and to a lesser degree Ca and Al. In protoplanetary disks, silicate dust is also observed in crystalline phase (Malfait et al., 1998, Bouwman et al., 2001, Meeus et al., 2001). Forsterite (Mg_2SiO_4) is the most abundant observable crystalline constituent in disks around T Tauri and Herbig Ae/Be stars (Olofsson et al., 2009, Juhász et al., 2010). Forsterite formation requires temperatures of $\gtrsim$ 1000 K (Hallenbeck et al., 2000, Fabian et al., 2000). At these temperatures, crystalline silicates can be formed through gas-phase condensation, and annealing of preexisting amorphous silicates (see Wooden et al. 2005 for an overview). The required temperatures indicate that forsterite forms in the inner disk. High crystallinity fractions in the inner disk have been confirmed by interferometric observations (van Boekel et al., 2004).

Even-though dust crystals are formed at high temperature and therefore close to the star, they have also been observed much farther away from the star than expected (Malfait et al., 1998, Olofsson et al., 2009, Juhász et al., 2010, de Vries et al., 2012, Sturm et al., 2013). Also in our own solar system, comets and interplanetary dust particles include crystalline silicates (MacKinnon & Rietmeijer, 1987, Bradley et al., 1992). Silicate grains in long-period comets like Hale-Bopp can be crystalline (Crovisier et al., 1997, Wooden et al., 1999, Harker et al., 2002). Laboratory measurements of olivine crystals from unequilibrated bodies (e.g. such as comet 81P/Wild 2, Zolensky et al. 2006; and cometary interplanetary dust particles Zolensky et al. 2008) are generally iron poor. Iron fractions (by number) in olivine crystals found in the Itokawa asteroid and in ordinary chondrites can be up to $\sim$ 30% (Nakamura et al., 2011). This may reflect the lack of large scale mixing (Shu et al., 1994, Bockelée-Morvan et al., 2002, Gail, 2004, Jacquet, 2014) and indicate the importance of crystal formation (i.e. local heating events) associated with the inner and outer disk region (Urey, 1967, Huss et al., 2001, Harker & Desch, 2002, Desch et al., 2005, Ábrahám et al., 2009, Morlok et al., 2010, Tanaka et al., 2010).

The transition from amorphous to crystalline silicate dust leads to strong changes in the optical response function of the material (Hallenbeck & Nuth, 1998). Crystalline silicates have several sharp solid-state features. Detailed analysis of these features provide a wealth of information on the properties of the crystal grains (Koike et al., 2003, Suto et al., 2006). As these properties can potentially be linked to the specific circumstances required to crystallise the dust grains, crystalline silicates allow us to probe physical processes changing the chemical compositions in the disk.

The width and peak position of the 69 μm feature of forsterite is sensitive to the temperature (Bowey et al., 2002, Suto et al., 2006, Koike et al., 2006). In addition, the peak position of the feature becomes red shifted for higher fractions of iron (Koike et al., 1993, 2003). Herschel observations using the Photodetector Array Camera and Spectrometer (PACS) has allowed to study the 69 μm feature with high spectral resolution (Sturm et al., 2010, Mulders et al., 2011, de Vries et al., 2012, Sturm et al., 2013). A detailed analysis of the 69 μm feature shapes in protoplanetary disks is presented in Sturm et al. (2013). These authors found the following results. Most of the forsterite grains that give rise to the 69 μm bands are found to be $\sim 100 - 200$ K and iron-poor (less than $\sim$2% iron), supporting the hypothesis that the forsterite grains form through an equilibrium condensation process at high temperatures. The large width of the emission band in some sources has been interpreted to indicate the presence of forsterite reservoirs at different temperatures. It was also concluded that any model that can explain the PACS and the Spitzer IRS observations must take the effects of a wavelength dependent optical depth into account.

Only for HD 100546 (Mulders et al., 2011), radiative transfer modeling has been performed to study the consistency between the relative mid-infrared band strengths and the information contained in the shape of the 69 μm band. It was found that the best solution is given by a model with a high abundance of forsterite located in the inner edge of the outer disk. As protoplanetary disks are highly optically thick media, radiative transfer modeling is essential to investigate optical depth effects and to simultaneously study the effects of grain growth, protoplanetary gaps and, radial mixing.

In this paper, we perform an in-depth study of the 69 μm feature of Herbig Ae/Be stars using radiative transfer models. We find that forsterite shows a variety of spectral characteristics for different groups of protoplanetary disks and we find that the detection rate of the 69 μm feature increases for lower disk masses (Section 6.2). As the different groups can be linked to physical processes in the disk, it shows that forsterite is a valuable tracer of the disk evolution history. In Section 6.3 we introduce the radiative transfer code and the dust model used in this study. We study the behaviour of forsterite in different evolutionary scenarios in Section 6.4. In Section 6.5 we present a case study of the peculiar 69 μm band which may be indicative for large grains originating in the optically thin disk of HD 141569. The discussion and conclusions are presented in Section 6.6 and 6.7, respectively.

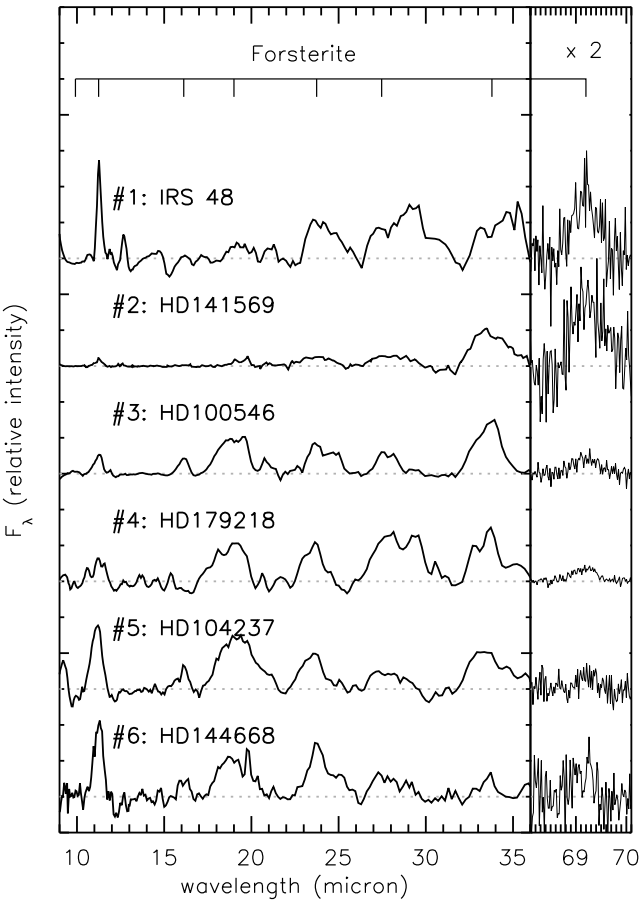

Figure 6.1: *Spectra of all sources with 69 μm detections. The continuum subtracted spectra are scaled relative to the strongest band. The objects are sorted by the $F_{30}/F_{13.5}$ ratio.*

6.2 Observations

In this section, we analyse the short and long wavelength forsterite features originating from protoplanetary disks. We compare the feature strength ratio I_{23}/I_{69} to the forsterite 69 μm shape and check for their consistency. In addition, we present trends between the I_{23}/I_{69} ratios and the millimetre (mm) luminosities of the disks. Note that throughout this paper, the integrated intensities are given by I_λ [erg cm^{-2} s^{-1}], the monochromatic flux by F_λ [erg cm^{-2} s^{-1} μm^{-1}], and the luminosity by L_λ [erg s^{-1}].

6.2.1 Data collection

We selected far-infrared (FIR) spectroscopic observations of Herbig stars (i.e. stars of spectral type F and higher) from the sample of Sturm et al. (2013). This allows us to identify trends in a sample of objects which are comparable in (stellar) properties. The observations were taken with the PACS instrument and are analysed as part of the Dust,

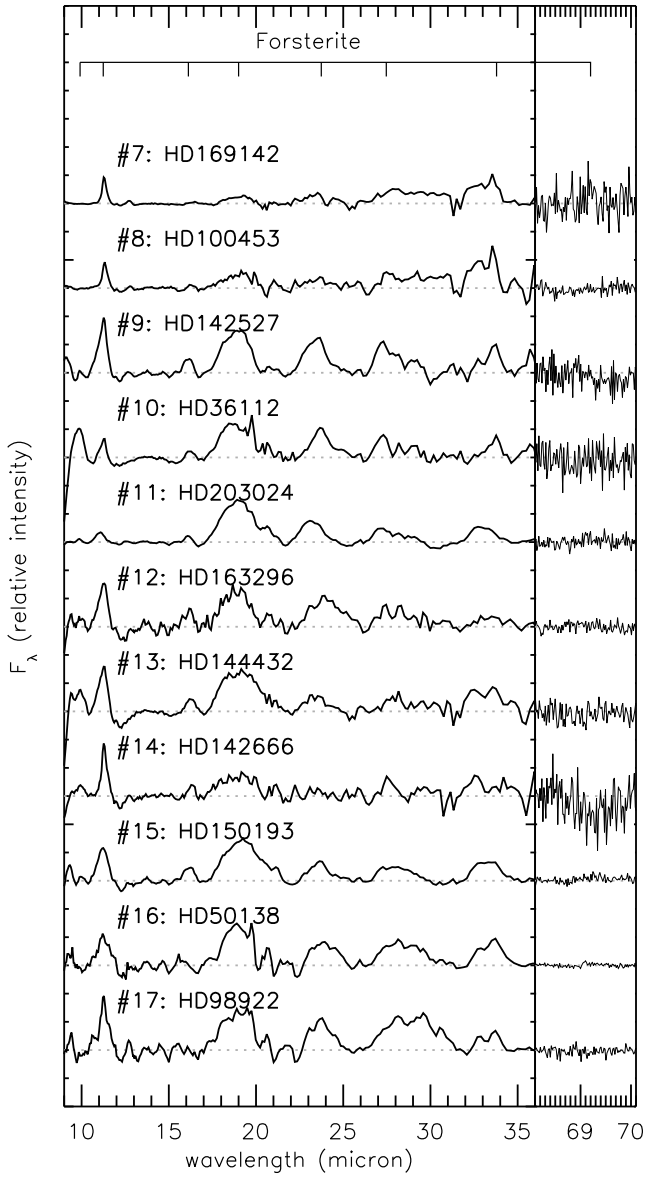

Figure 6.2: *Spectra of all sources with three or more forsterite features detected in the Spitzer/IRS spectrum. These objects have no detections at 69 μm. The continuum subtracted spectra are scaled relative to the strongest band and the objects are sorted by the $F_{30}/F_{13.5}$ ratio.*

Ice and Gas in Time (DIGIT) Herschel key programme. The data is processed using the Herschel Interactive Processing Environment (HIPE) using calibration version 42 and standard pipeline scripts. Table 6.1 shows the properties of the objects with forsterite 69 μm detections. Table 6.2 shows all Herbig Ae/Be objects which have been observed. For comparison with the spectral energy distributions (SEDs) we collected fluxes at 13.5 and 30 μm from Acke et al. (2010) and mm photometry for all sources from the literature. Identification of forsterite features in the wavelength range between $\sim 15-35$ μm is done using Spitzer/IRS spectra, which were first published by Juhász et al. (2010) and

re-reduced by the most recent calibration version (S18.18.0) for the study of Sturm et al. (2013).

Identification and measurements of the forsterite features are carried out after fitting and subtracting the continuum. The best fit to the continuum is obtained using a spline function, which is a polynomial between continuum wavelengths chosen just outside the features. The best results were obtained using the following wavelengths for the continuum. For the Spitzer/IRS wavelength domain: $\lambda_{\text{continuum}} = \{5.52, 5.83, 6.66, 7.06, 9.54, 10.32{,}12, 13.08, 13.85, 15.00, 17.00, 21.75, 26.00, 31.60, 35.10, 36.01\}$ μm. For the Herschel/PACS wavelength domain: $\lambda_{\text{continuum}} = \{65.50, 67.50, 68.55, 69.70, 70.00, 70.50, 71.00, 71.50\}$ μm. At each point we took the average continuum flux for a small wavelength range ($\Delta\lambda \sim 1\mu$m) around the feature. An extended discussion of this approach is given in Appendix B of Mulders et al. (2011). We visually checked that the continuum was properly fitted so that the strengths of the forsterite features could be accurately determined. We checked the spectra for detections of forsterite features. Almost all of the forsterite features we identify are also reported in Juhász et al. (2010) and Sturm et al. (2013). Table 6.2 gives an overview of all forsterite detections (for the short wavelength features, this implies that at least three bands are identified). Finally, the 23 μm feature is identified using a χ^2 Gaussian fitting routine and thereafter integrated to determine the band strengths. From all the short wavelength features we choose the 23 μm band for analysis because: 1) the band is relatively unaffected by the amorphous silicate feature, 2) it is a strong/prominent band, 3) there is minimal interference of other crystalline silicate bands (most notably enstatite) and 4) the Spitzer/IRS observations are reliable at that wavelength range. The error on the flux of the 23 μm band is dominated by the choice of the continuum points next to the features. This error calculation varies the position of the continuum points by a Monte Carlo based method and determines the 1 σ deviation to the mean flux. We derive a typical error of $\sim$20% to the feature strength.

Sturm et al. (2013) report the detection of the 69 μm feature in the PACS spectrum of AB Aur. However, several indications make the detection uncertain. The identification of the continuum between $\sim 65-75$ μm is arbitrary since the continuum of AB Aur shows several bumps in this wavelength range. Due to instrumental issues with PACS, it is not easy to identify for the indicated wavelength range if bumps are instrumental artefacts, real features or continuum. After analysis of the 69 μm the shape, the reported forsterite feature has a peculiar square-like shape, which is not seen in the other detections of the Herbig stars. In addition, the peak position is redshifted by 0.8 μm, while the other detections are all within a range of 0.2 μm. While this could be an effect of an iron fraction of $\sim$4 %, it is somewhat peculiar that AB Aur has this iron fraction, and the other detections not. Finally, unlike all other Herbig stars where the 69 μm feature is detected, AB Aur has no sign of forsterite detections in the Spitzer/IRS spectrum. Therefore, we choose not to classify the 69 μm feature of AB Aur as a detection of forsterite into our analysis. We emphasize that AB Aur is an outlier and better observations are needed to confirm the detection with sufficient confidence.

6.2.2 New Meeus group classication based on the $F_{30}/F_{13.5}$ continuum flux ratio

Meeus et al. (2001) showed that the SEDs of Herbig stars can be divided in two typical groups: sources with a strong mid-to far-infrared excess (group I) and sources which can be fitted by just one powerlaw (group II). A strong correlation between the $F_{30}/F_{13.5}$ continuum flux ratio and the group classification based on Meeus et al. (2001) has been shown in Maaskant et al. (2013, 2014). Group I and II sources have respectively high and low $F_{30}/F_{13.5}$ ratios and are easily distinguished by this parameter. Larger sizes of the gap in the disk temperature regime between $\sim 200-500$K causes the continuum flux at 13.5 μm to decrease. However, because the inner edge of the outer disk is a vertical wall with a high surface brightness, the flux at 30 μm increases. Therefore high values of $F_{30}/F_{13.5}$ are indicative of large gap sizes (Maaskant et al., 2013). As proposed by Khalafinejad (in prep.) the transitions between Meeus groups Ia, Ib and group IIa can be more easily classified using the $F_{30}/F_{13.5}$ ratio. With geometrically flat, full disks showing amorphous silicate features (group IIa): $F_{30}/F_{13.5} \leqslant 2.1$. For transitional/flaring objects with amorphous silicate features (group Ia): $2.1 < F_{30}/F_{13.5} < 5.1$. The transitional/flaring objects which do not have silicate features (group Ib) have: $F_{30}/F_{13.5} \geqslant 5.1$. The devision of these groups can be seen in Figure 6.3. The absence of the silicate feature is correlated with the highest values of $F_{30}/F_{13.5}$ because the disk gap is significantly depleted in small silicate dust grains. Due to the depletion of small dust grains, the optical depth also decreases, which enhances the flux from smaller PAH molecules which are thought to travel along with the gas (Maaskant et al., 2014). For our study we adopt this new classification scheme of the Meeus groups based on the $F_{30}/F_{13.5}$ ratio.

6.2.3 Properties of the forsterite features

Out of 23 sources observed with Herschel/PACS, 6 objects have a detection of the 69 μm feature. Their continuum subtracted Spitzer/IRS and Herschel/PACS spectra are shown in Figure 6.1. All objects without 69 μm feature detections are shown in Figure 6.2. In these figures, the continuum subtracted spectra are scaled relative to the strongest forsterite band and the objects are sorted by the continuum feature strength ratio of the 30 μm and 13.5 μm features (i.e. the $F_{30}/F_{13.5}$ ratio). We could not identify any parameters that could explain the lack of forsterite features for several sources (sources #18 – #23, see Table 6.2).

6.2.4 Observational trends

Since we only have a very small number of 69 μm detections, extracting trends is difficult and we should be careful drawing strong conclusions. Nevertheless, we searched for trends between the forsterite features and the stellar and photometric properties. The following tentative trends, related to the photometric properties (Figure 6.3) and to the forsterite features (Figure 6.4), could be identified in the data.

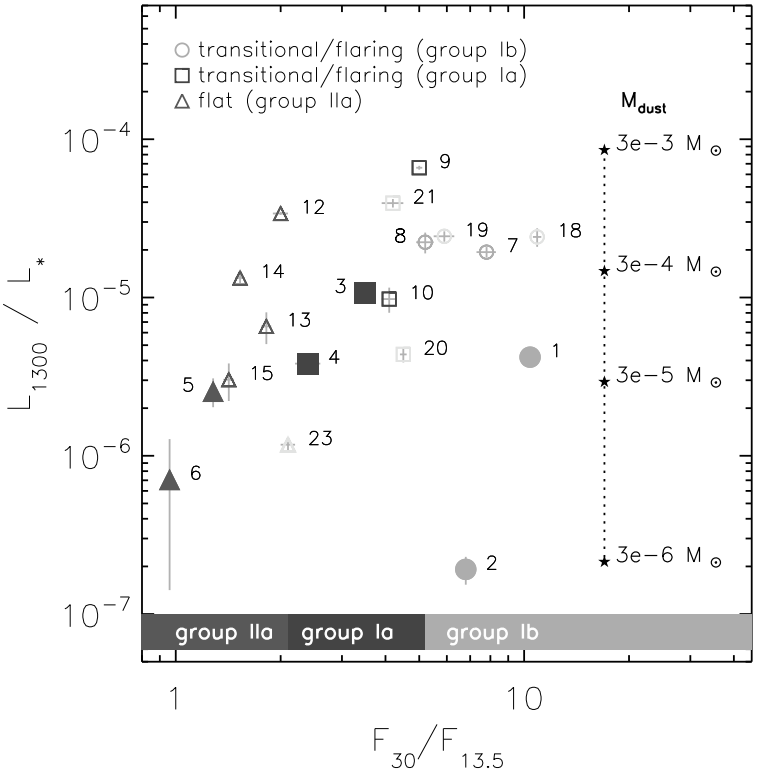

Figure 6.3: *The disk luminosity at 1.3 mm (L_{1300}/L_*) compared to the MIR spectral index $F_{13.5}/F_{30}$ ratio. Filled symbols indicate the objects for which the 69 μm feature has been detected. The 69 μm feature is often detected for disks with low L_{1300}/L_*. The MIR spectral index can be used as a tracer of large disk gaps. The symbols show flaring/transitional disks without silicate features (group Ib, circles, $F_{30}/F_{13.5} \geqslant 5.1$), with silicate features (group Ia, squares, $2.1 < F_{30}/F_{13.5} < 5.1$), and self-shadowed disks with silicate features (group IIa, triangles, $F_{30}/F_{13.5} \leqslant 2.1$). The numbers refer to the objects and are given in Table 6.2. The grey symbols show the objects with no forsterite detections at Spitzer/IRS and Herschel/PACS wavelengths.*

Figure 6.3 shows all the Herbig stars which have been observed with Spitzer/IRS and Herschel/PACS. This plot relates the 69 μm detections to the photometric properties of the Herbig stars. One of the main indicators of the protoplanetary disk mass is the 1.3 mm optically thin dust continuum emission. For comparison we have over-plotted mm luminosities of a radiative transfer modeling grid were the mass is varied by 4 orders of magnitude (section 6.4.5). This plot shows that the detection rate of the 69 μm forsterite features tends to be higher for lower 1.3 mm luminosities (L_{1300}/L_*). Thus for lower mass disks, the 69 μm feature seems to be more frequently detected (69 μm detections indicated by the filled symbols). We will discuss in Section 6.4 which disk evolutionary scenarios can explain this behaviour. Figure 6.3 also shows that there is no correlation between the 69 μm detections and the presence of large gaps as indicated by the MIR spectral index $F_{30}/F_{13.5}$ ratio.

Figure 6.4 shows all the sources with forsterite detections in the Spitzer/IRS and/or

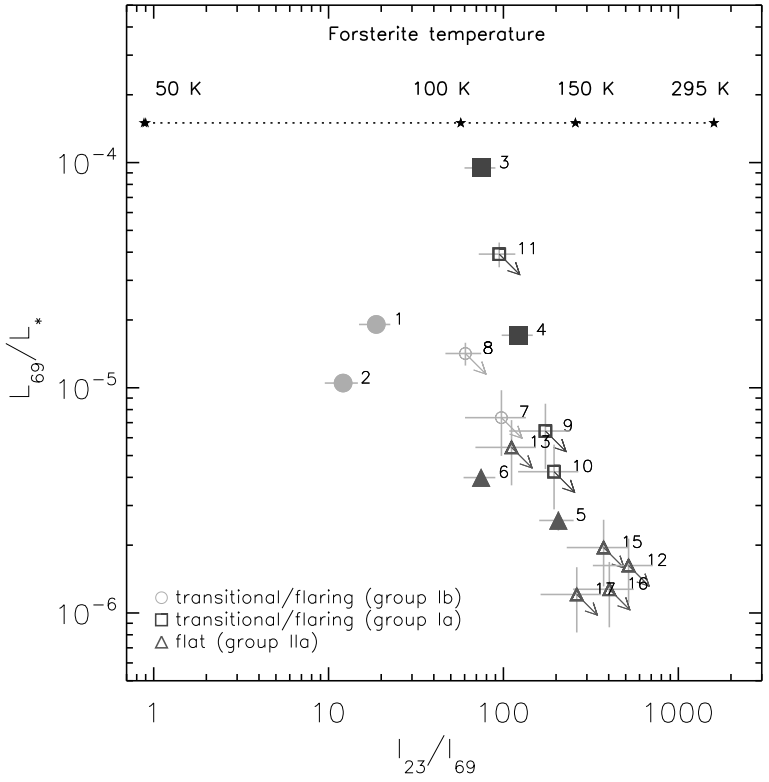

Figure 6.4: *The luminosity of the 69 μm feature (L_{69}/L_*) compared to the I_{23}/I_{69} ratio. Filled symbols indicate the objects for which the 69 μm feature has been detected. The numbers refer to the objects and are given in Table 6.2. The arrows indicate the upper limits of the 69 μm feature. The stars indicate band strength ratios of temperature dependent forsterite opacities multiplied by black bodies of corresponding temperatures. Thus the emission profile of optically thin dust emission is modelled and serves as a simple first comparison to the observed features ratios.*

Herschel/PACS wavelength range. It relates the 69 μm luminosity to the Meeus groups as well as to the forsterite temperature. Note that the absolute feature strength *alone* is a difficult diagnostic tool to search for processes in disks because the abundance differences are important for it and there is a large dispersion in the crystallinity fractions of Herbig stars. The I_{23}/I_{69} band strength *ratio* can be interpreted as a probe of the dominant forsterite temperature in the disk because it measures the shape of the underlying blackbody. Also overlaid are feature strength ratios for optically thin representative dust mixtures of different temperatures (20% forsterite, 20% amorphous carbon and 60% amorphous silicates, see Section 6.3.1 for the description of the dust model). In this mixture, temperature dependent opacities of forsterite are adopted (Suto et al., 2006). Hence, a high I_{23}/I_{69} ratio reflects a high forsterite temperature. We can learn from this plot that the luminosity of the 69 μm detections is stronger for transitional/flaring disks (group I) compared to the self-shadowed/flat (group II) objects. In addition, the forsterite temperature indicator I_{23}/I_{69} seems to be $\sim 1-2$ orders of magnitude lower for the group Ib objects (Oph IRS 48 and HD 141569) than for group Ia and IIa objects. The weakest detections of the 69 μm feature are found for the flat (group II) objects and have a similar I_{23}/I_{69} ratio as group Ia

objects. In the majority of objects, the 69 μm feature is not observed. The non-detection could be a consequence of insufficient sensitivity (such as for object #11: HD 203024). However, for the flat (group II) objects on the bottom right corner of Figure 6.4 (#12, #15, #16 and #17), the 23 μm feature is strong compared to the upper limit of the 69 μm feature. For these objects we can conclude that the forsterite temperature must be high.

The possible effects of these trends on the relative band strength I_{23}/I_{69} and the 69 μm width and peak position will be carefully examined in the remainder of this paper.

6.2.5 Consistency between feature strength ratio I_{23}/I_{69} and the 69 μm band shape

Another independent way of estimating the forsterite temperature relies on the analysis of the 69 μm feature shape. The features width and peak position contains information about the temperature, iron fraction and grain size. We will now check the consistency between both methods to derive a forsterite temperature estimate.

The feature strengths, widths and peak positions of the 69 μm feature are examined in Sturm et al. (2013). The feature properties are shown in Table 6.1. Lorentzian fits are also derived for the features to be able to compare them to the detection of the 69 μm feature in Beta Pictoris presented in de Vries et al. (2012). The forsterite in the debris disk of Beta Pictoris was found to be ∼80 K at a distance of ∼40 AU, and contains 1% iron. As gas rich disk may eventually evolve into debris disks, a comparison between the properties of the 69 μm feature in Herbig stars to that of Beta Pictoris may be relevant. The feature widths and positions for the sources in our sample are shown in Figure 6.5. The average width is ∼0.28 μm and the average peak position is ∼69.2 μm. Over-plotted are laboratory are measurements from Suto et al. (2006) with an iron fraction of 0% (right solid line). The right dashed line gives the widths and peak positions of 1% iron fraction; these are interpolated between 0% and 8% iron fractions using a linear trend fitted (de Vries et al., 2012) to the measured values between 0% and 16% iron fractions from Koike et al. (2003). The 69 μm feature shapes of protoplanetary disks are similar to laboratory measurements of $\sim 150-200$ K forsterite with an iron fraction between $0-1\%$.

The I_{23}/I_{69} ratio and the 69 μm band shapes are not consistent for HD 100546, HD 144668, HD 141569 and Oph IRS 48. Thus, a single temperature analysis can not explain the difference in the observational appearance of forsterite and more complex models have to be invoked. We will show in Sections 6.3 and 6.4 that the I_{23}/I_{69} ratio and the 69 μm band shape is sensitive to (distributions) of temperatures, iron fractions, grain sizes and optical depth effects. For HD 100546, it has been shown that the difference in temperature indicators can be explained by optical depth effects which increases the strength of the 69 μm feature compared to the 23 μm feature because the disk is optically thinner at longer wavelength (Mulders et al., 2011). Possibly a similar scenario may be the case for HD 144668. However, for the evolved transitional disks HD 141569 and Oph IRS 48, such optical depth effects are not sufficient since these disks are much more optically thin. Their very weak short wavelength features suggest that the forsterite must be cold ($T \lesssim 90$

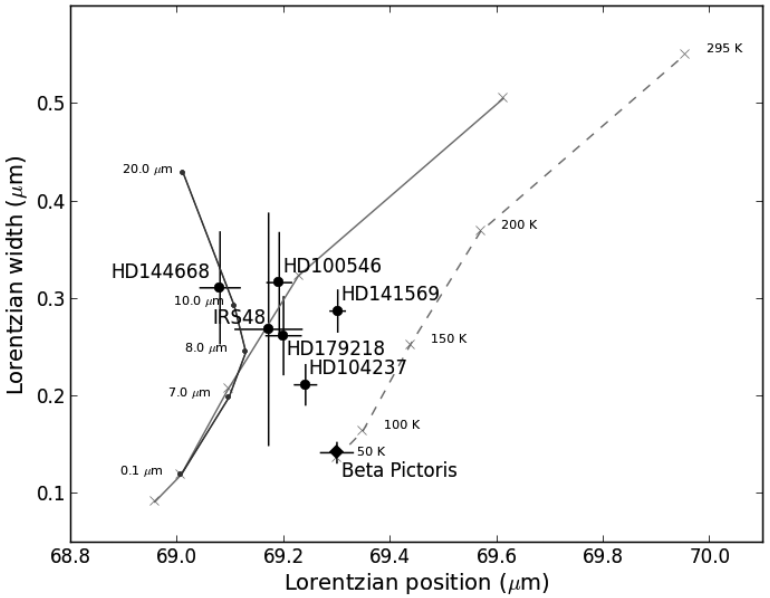

Figure 6.5: *Lorentzian width versus peak position diagram of 69 micron features (Gaussian values in Table 6.1). The left solid line shows the peak positions and widths for a T = 100 K grain with increasing size between 0.1* μm *and 20* μm*, computed with distribution of hollow spheres (DHS). The left solid grey line represents the peak positions and widths for iron free forsterite and increasing temperatures of 50 K, 100 K, 150 K, 200 K and 295 from laboratory measurements of Suto et al. (2006). The right dashed grey line shows the interpolated shift in peak position of the 69* μm *feature. The right dashed grey line shows the interpolated shift in peak positions and widths for the 69* μm *feature for 1% iron fraction(Koike et al., 2003).*

K). However, the band shape of their 69 μm features suggests much higher temperatures (respectively 174 K and 156 K, Sturm et al. 2013). In Section 6.5, we perform a case study of HD 141569 and present forsterite models which can fit the short and long wavelength spectra.

6.3 Radiative transfer and dust model

Many physical assumptions are made in models of dust features from protoplanetary disks. In this section we explain our modeling approach. First we discuss the dust model used for the analysis of forsterite features. Thereafter we briefly explain how forsterite is implemented in the radiative transfer code MCMax (Min et al., 2009) .

Table 6.1: *Peak positions and widths given for Lorentzian and Gaussian fits. For clarity, they are both given so that they are comparable to the Lorentzian values derived for Beta Pic (de Vries et al., 2012). Gaussian values are taken from Sturm et al. (2013). The difference between Lorentzian and Gaussian widths stems from their definition.*

ID	Object	p_L (μm)	w_L (μm)	p_G (μm)	w_G (μm)
1	Oph IRS 48	69.170	0.269	69.168	0.521
2	HD141569	69.300	0.288	69.303	0.600
3	HD100546	69.191	0.317	69.194	0.681
4	HD179218	69.199	0.262	69.196	0.502
5	HD104237	69.240	0.212	69.224	0.351
6	HD144668	69.079	0.312	69.088	0.599

Table 6.2: *The sample of Herbig stars studied in this paper. $\uparrow$ indicates upper limits. References of mm photometry are given in Table 1 of Maaskant et al. 2014.*

ID #	Target	Spitzer detections	69 µm detection	$F_{30}/F_{13.5}$ ∇	group	I_{23} erg cm^{-2} s^{-1}	I_{69} erg cm^{-2} s^{-1}	L_* $L_\odot$	T_* K	d pc	F_{1300} mJy
1	Oph IRS 48	√	√	10.40 ± 0.30	Ib	$1.14 \pm 0.21 \times 10^{-11}$	$6.11 \pm 0.21 \times 10^{-13}$	14.3	10000	120	60 ± 10
2	HD 141569	√	√	6.80 ± 0.20	Ib	$7.67 \pm 1.53 \times 10^{-12}$	$6.32 \pm 0.49 \times 10^{-13}$	18.3	9520	99	5 ± 1
3	HD 100546	√	√	3.50 ± 0.20	Ia	$7.08 \pm 1.40 \times 10^{-10}$	$9.46 \pm 0.13 \times 10^{-12}$	32.9	10500	103	465 ± 20
4	HD 179218	√	√	2.40 ± 0.20	Ia	$8.97 \pm 1.79 \times 10^{-11}$	$7.33 \pm 0.18 \times 10^{-13}$	79.2	9810	244	71 ± 7
5	HD 104237	√	√	1.28 ± 0.03	IIa	$4.41 \pm 0.88 \times 10^{-11}$	$2.14 \pm 0.21 \times 10^{-13}$	34.7	8405	116	92 ± 19
6	HD 144668	√	√	0.96 ± 0.02	IIa	$1.93 \pm 0.38 \times 10^{-11}$	$2.60 \pm 0.13 \times 10^{-13}$	87.5	7930	208	20 ± 16
7	HD 169142	√	…	7.80 ± 0.50	Ib	$1.68 \pm 0.34 \times 10^{-11}$	$\uparrow 1.73 \pm 0.56 \times 10^{-13}$	15.3	8200	145	197 ± 15
8	HD 100453	√	…	5.20 ± 0.30	Ib	$1.77 \pm 0.35 \times 10^{-11}$	$\uparrow 2.93 \pm 0.34 \times 10^{-13}$	8.0	7390	112	200 ± 31
9	HD 142527	√	…	5.00 ± 0.10	Ia	$4.64 \pm 0.92 \times 10^{-11}$	$\uparrow 2.67 \pm 0.86 \times 10^{-13}$	50.6	6260	198	1190 ± 33
10	HD 36112	√	…	4.10 ± 0.20	Ia	$1.40 \pm 0.28 \times 10^{-11}$	$\uparrow 7.20 \pm 2.30 \times 10^{-14}$	22.2	7850	205	72 ± 13
11	HD 203024	√	…	2.30 ± 0.20	Ia	$3.08 \pm 0.62 \times 10^{-11}$	$\uparrow 3.26 \pm 0.41 \times 10^{-13}$	99.2	8200	620	…
12	HD 163296	√	…	2.00 ± 0.10	IIa	$4.26 \pm 0.85 \times 10^{-11}$	$\uparrow 8.20 \pm 2.60 \times 10^{-14}$	23.3	8720	122	743 ± 15
13	HD 144432	√	…	1.82 ± 0.06	IIa	$9.36 \pm 1.90 \times 10^{-12}$	$\uparrow 8.40 \pm 2.70 \times 10^{-14}$	10.1	7345	145	44 ± 10
14	HD 142666	√	…	1.53 ± 0.05	IIa	$\uparrow 1.73 \pm 0.35 \times 10^{-12}$	$\uparrow 6.53 \pm 2.11 \times 10^{-13}$	14.4	7580	145	127 ± 9
15	HD 150193	√	…	1.42 ± 0.05	IIa	$2.50 \pm 0.50 \times 10^{-11}$	$\uparrow 6.70 \pm 2.20 \times 10^{-14}$	24.0	8990	150	45 ± 12
16	HD 50138	√	…	0.78 ± 0.04	IIa	$8.38 \pm 1.67 \times 10^{-11}$	$\uparrow 2.08 \pm 0.67 \times 10^{-13}$	423.5	12230	289	…
17	HD 98922	√	…	0.75 ± 0.03	IIa	$3.01 \pm 0.25 \times 10^{-11}$	$\uparrow 1.15 \pm 0.37 \times 10^{-13}$	855.7	10500	538	…
18	HD 135344 B	…	…	10.90 ± 0.30	Ib	$\uparrow 3.72 \pm 0.74 \times 10^{-13}$	$\uparrow 1.12 \pm 0.36 \times 10^{-13}$	8.3	6590	140	142 ± 19
19	HD 97048	…	…	5.90 ± 0.40	Ib	$\uparrow 9.80 \pm 1.90 \times 10^{-12}$	$\uparrow 1.96 \pm 0.63 \times 10^{-13}$	40.7	10010	158	452 ± 34
20	AB Aur	…	…	4.50 ± 0.10	Ia	$\uparrow 2.19 \pm 0.43 \times 10^{-11}$	$\uparrow 1.01 \pm 0.09 \times 10^{-12}$	46.2	9520	144	136 ± 15
21	HD 139614	…	…	4.20 ± 0.30	Ia	$\uparrow 2.18 \pm 0.43 \times 10^{-12}$	$\uparrow 7.50 \pm 2.40 \times 10^{-14}$	8.6	7850	140	242 ± 15
22	HD 38120	…	…	2.60 ± 0.20	Ia	$\uparrow 4.03 \pm 0.81 \times 10^{-12}$	$\uparrow 6.00 \pm 1.90 \times 10^{-14}$	89.3	10500	510	…
23	HD 35187	…	…	2.10 ± 0.10	IIa	$\uparrow 8.35 \pm 1.60 \times 10^{-13}$	$\uparrow 1.98 \pm 0.23 \times 10^{-13}$	27.4	8970	150	20 ± 2

6.3.1 Dust model

Throughout this paper, we make use of a standard dust composition responsible for the continuum radiation of 80% silicate and 20% amorphous carbon. This is the dust component without forsterite. To be consistent with previous radiative transfer modeling by Mulders et al. (2011), the adopted amorphous dust composition with reference to the optical constants, is 32% $MgSiO_3$ (Dorschner et al., 1995), 34% Mg_2SiO_4 (Henning & Stognienko, 1996), 12% $MgFeSiO_4$ (Dorschner et al., 1995), 2% $NaAlSi_2O_6$ (Mutschke et al., 1998), 20% C (Preibisch et al., 1993). The shape of our particles is irregular and approximated using a distribution of hollow spheres (DHS, Min et al. 2005) using a maximum vacuum fraction $f_{max} = 0.7$. In DHS, f_{max} is the parameter which controls the shape of the particle and can be regarded as the 'irregularity' parameter, as there is no observable difference between porosity and irregularity.

Forsterite features are analysed using the optical constants from laboratory data of Suto et al. (2006) and using irregular DHS particles with a maximum vacuum fraction of $f_{max} = 0.7$, which has been found to be a good representation of observed short wavelength crystalline silicate profiles in Spitzer data (Juhász et al., 2010). The effects of temperature on the width and peak position of the 69 μm feature are also illustrated in Figure 6.5. The forsterite opacities of Suto et al. (2006) are temperature dependent, and are the best opacities available to use in radiative transfer modeling of protoplanetary disks where the temperatures are below $\lesssim$ 1500 K. Figure 6.6 shows the opacities of several forsterite grains. The top figure shows 1 μm grains for 50 K and 295 K. The short wavelength features are very similar, while the peak strength, peak position, and width of the 69 μm feature are very sensitive to the temperature in this range. The integrated feature strength of the 69 μm feature is ∼3 times higher for 50 K compared to 295 K forsterite. The bottom figure shows the opacities of 1 and 10 μm grains. Due to the larger grain size, the grain model predicts that the shorter wavelength features become weaker, and that the 69 μm feature broadens. A more detailed discussion on the emission characteristics of larger (∼ 10 μm) forsterite grains is given in Min et al. (2004). The temperatures of amorphous silicates and carbonaceous grains are calculated from radiative equilibrium. It is assumed that the forsterite grains are in thermal contact with the other dust constituents. Where relevant, we evaluate in the next sections whether this assumption is reasonable. See Mulders et al. (2011) for an extended discussion on the assumption of thermal contact between the dust grains in radiative transfer modeling of protoplanetary disks.

6.3.2 Radiative transfer model

We use the Monte Carlo radiative transfer code MCMax to compute full radiative transfer models. With a given set of star and disk input parameters, MCMax can compute the temperature and the vertical density structure of highly optically thick disks self-consistently. From these models it produces a range of observables such as the resulting SED and the forsterite features which are calculated by integrating the formal solution to the equation of radiative transfer by ray-tracing.

6.4 Benchmark modeling

In this section, we construct a benchmark model for a typical disk around a Herbig star. This model is used to investigate the key parameters that change the feature strength ratio of forsterite in protoplanetary disks. The aim is to provide a qualitative description for the behaviour of the feature strength ratio I_{23}/I_{69}. Thereby, we derive estimates of the minimum and maximum I_{23}/I_{69} ratios and compare them to the observed values in the spectra of the objects in our sample. We start by introducing the properties of a benchmark disk model. We study four evolutionary disk scenarios that control the I_{23}/I_{69} band strength ratio: **1)** grain growth, **2)** transitional disk, **3)** radial mixing and **4)** optical depth effects.

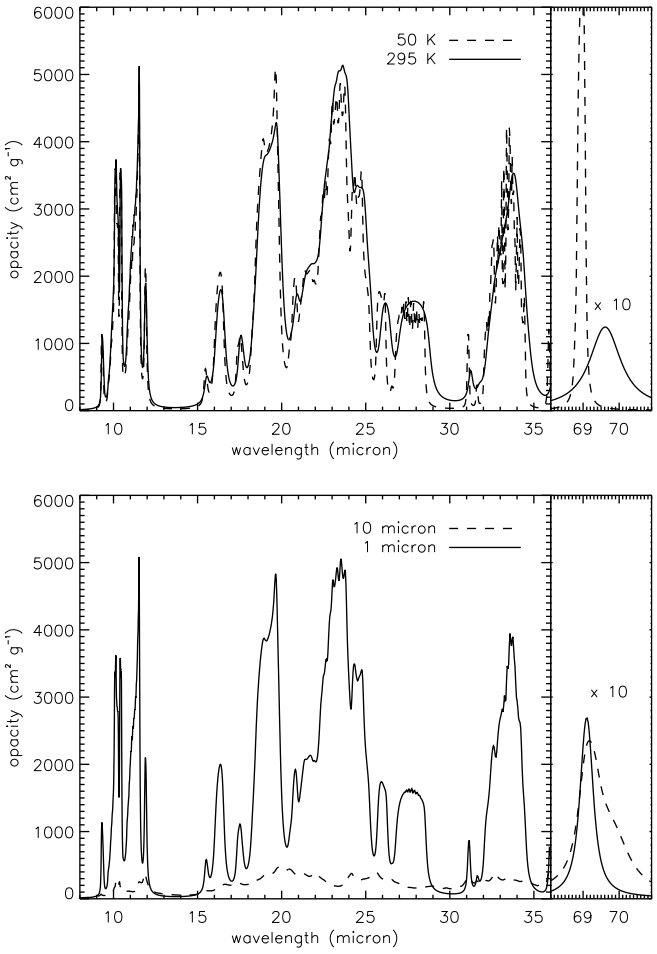

Figure 6.6: *Top: calculated opacities of 1 μm forsterite grains at 50 K and 295 K. Bottom: calculated opacities for 1 and 10 μm forsterite grains (T = 150 K).*

6.4.1 Benchmark disk model

We model a hydrostatic flaring disk with stellar properties from HD 97048 (see parameters in table 6.2). The parameters of this model are taken from the study of Maaskant et al. (2014) and summarized here (see Table 6.3). The chosen stellar properties ($L_* = 40.7 L_\odot$, $T_* = 10010$ K) are typical for Herbig Ae/Be stars. By this choice, the influence of the stellar radiation to the thermal structure of the disk can be assumed to represent the objects in our sample. The inner and outer radii of the disk are set at respectively 0.1 and 250 AU. The radial dependence of the surface density is parametrised by a power law with index -1. The dust mass is $M_{dust} = 3 \times 10^{-4}$ $M_\odot$, where we assume a gas-to-dust ratio of 100. The dust size ranges from $a_{min} = 0.01$ μm up to $a_{max} = 1$ mm and follows a power-law distribution with $a_{pow} = -3.5$.

The standard benchmark model described above does not yet contain forsterite. The models presented in the following sections are different from the benchmark model because forsterite is added to the disk between given radii. This is done by replacing a mass fraction of 10% of the standard dust component by forsterite grains. Note that the total

dust mass at any radius is therefore conserved and that the forsterite grains used in the models are all one size and iron free. Additionally, in the scenarios *transitional disk* and *optical depth*, also the disk parameters $R_{in,disk}$ (inner radius of the disk) and $M_{dust,disk}$ (disk mass in dust) are changed to better mimic the disk evolutionary scenarios. All other parameters are held constant so that the effect of the changed parameter is best visible.

Table 6.3: *Characteristics of the benchmark model.*

Parameter		Unit	Benchmark
Stellar temperature	T_*	K	10 010
Stellar luminosity	L_*	$L_\odot$	40.7
Stellar radius	R_*	$R_\odot$	2.12
Stellar mass	M_*	$M_\odot$	2.50
inclination	i	$^\circ$	45
Distance	d	pc	158
Disk, inner radius	$R_{in,disk}$	AU	0.1
Disk, outer radius	$R_{out,disk}$	AU	250
Silicate fraction	f_{Si}	...	0.8
Carbon fraction	f_C	...	0.2
Min dust size	a_{min}	µm	0.01
Max dust size	a_{max}	mm	1
Dust-size power-law index	a_{pow}	...	-3.5
Disk, gas mass	$M_{gas,disk}$	$M_\odot$	3.0×10^{-2}
Disk, dust mass	$M_{dust,disk}$	$M_\odot$	3.0×10^{-4}

6.4.2 Scenario 1: grain growth

In the scenario *grain growth*, the dependence of the relative features strengths on the grain size is studied. We compare forsterite grains of 1, 5 and 10 µm in size. In this modeling grid, forsterite is mixed in the region between $0-50$ AU. As shown by the opacities in Figure 6.6, for grains $\gtrsim 1$ µm, the shorter wavelength features get weaker compared to the 69 µm feature. Thus I_{23}/I_{69} also decreases. For grains smaller than a few micron, the relative band strength is constant. Because the features between $25-35$ µm change in position, the points where the continuum is subtracted is changed from 21.75 and 26.4 µm to 23.5 and 29 µm.

6.4.3 Scenario 2: transitional disk

The scenario *transitional disk* highlights the temperature dependence of the feature strength ratios. To model this, we create disk models with increasingly larger inner holes (50, 100, and 150 AU). We then assume in each transitional disk that forsterite is present (10 %) in

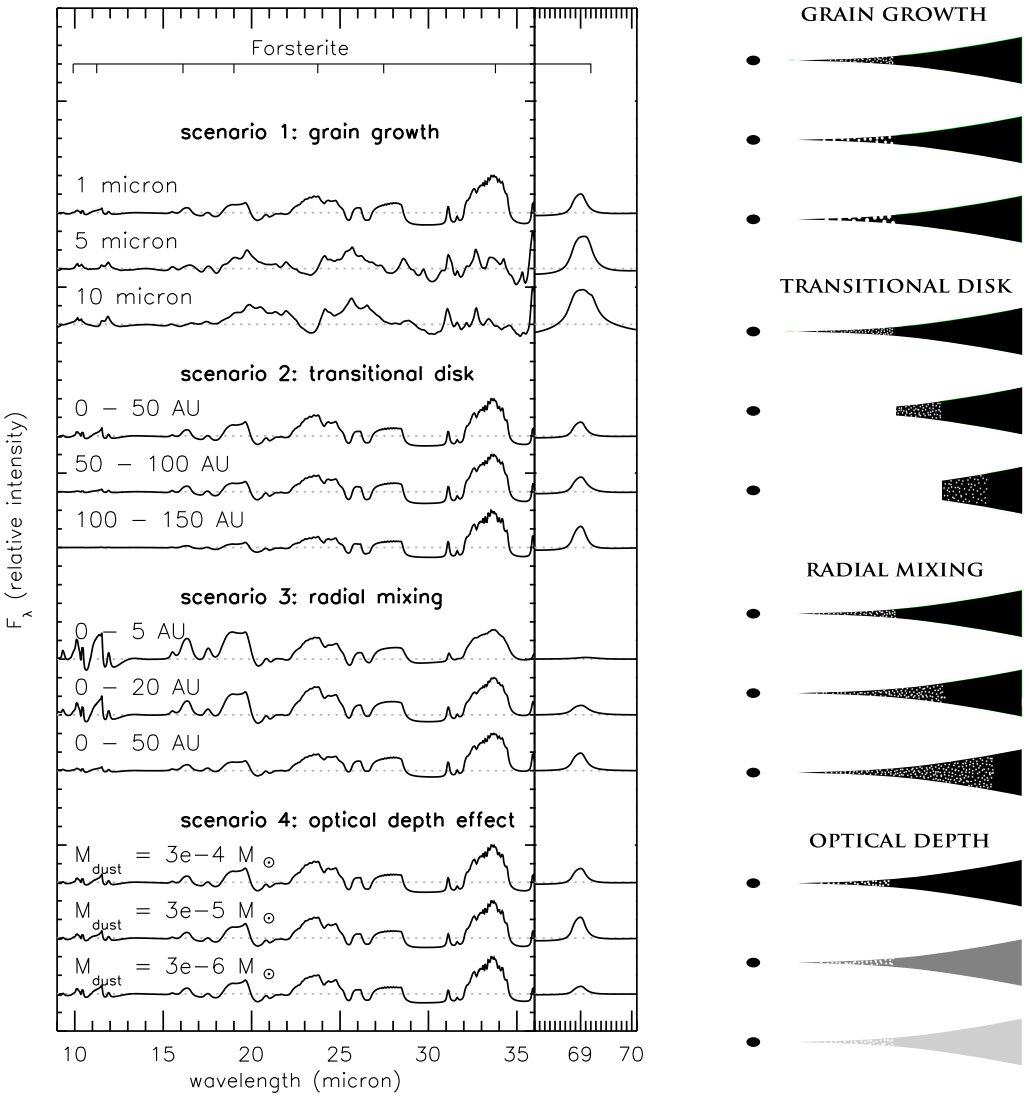

Figure 6.7: *Grain size scenario, transitional disk scenario, radial mixing scenario, optical depth effect. The continuum subtracted spectra are scaled relative to the strongest band so that the effect on the forsterite temperature is presented best. The right panel shows sketches to illustrate the structure of the disk and the location and sizes of forsterite grains.*

the 50 AU-wide region just outside of the gap. For the disk as a whole this means that an increasing amount of near infrared continuum is missing. The dominant effect for the forsterite feature ratios is the temperature selection that is taking place.

6.4.4 Scenario 3: radial mixing

The effect of forsterite being gradually mixed towards larger radii is studied in the scenario *radial mixing*. To model this scenario, a forsterite mass abundance of 10% is mixed in

the disk between 0.1 AU up to 5, 20 and 50 AU. When forsterite is mixed with a constant mass abundance ratio up to 50 AU in the disk, the feature strength ratio is $I_{23}/I_{69} = 1.2$. If forsterite is only present in the inner disk within 5 AU, than the 69 μm feature is relatively weak and $I_{23}/I_{69} = 15.2$.

6.4.5 Scenario 4: optical depth effects

The scenario *optical depth effects* investigates the feature strength ratio as a result of the differences in dust continuum optical depth. The optical depth is lower at longer wavelengths, therefore the $\tau = 1$ surface at 69 μm lies deeper in the disk than the $\tau = 1$ surface at 23 μm. Hence, the regions in the disk producing the 23 and 69 μm features have different volumes. Thus the feature strength ratio can be altered if the optical depth changes in the disk (as shown for HD 100546 in Mulders et al. 2011). We model this scenario adopting a mass abundance of 10% of forsterite within $0-50$ AU in the disk, and by varying the mass of the disk between 3×10^{-4} $M_\odot$ and 3×10^{-6} $M_\odot$. By decreasing the total mass in the disk, the disk goes stepwise from optically thick at both 23 and 69 μm to optically thin at 69 μm, and on to optically thin in both features. The 1.3 mm luminosity values of these disk models are over-plotted on Figure 6.3 and cover the range of observed 1.3 mm continuum detections for our sample of Herbig stars.

6.4.6 Summary of modelling scenarios

Comparing the results in this section to the observations as presented in Table 6.2 and Figures 6.4 and 6.3 we obtain the following results.

Since grains grow in protoplanetary disks, the *grain growth* scenario may be important to explain the observed forsterite feature strength ratios. Figure 6.7 shows the relative band strengths for different grain sizes. We find that for 1 μm grains the I_{23}/I_{69} band strength ratio is highest. For grains larger than a few micron, we find that the 23 μm band disappears and thus that the I_{23}/I_{69} ratio decreases to zero. For one particular object, HD 141569, it is demonstrated in Section 6.5, that the grain size is a plausible explanation for the feature strength ratio. Dust settling and grain growth of the standard dust component are not included. In reality, other grains also grow in size, and larger grains settle towards the midplane leaving relatively more small dust grains in the surface layers of the disk. These effects mainly affect the optical depth of the disk. Therefore, grain growth and settling change the ratio of flux contributions from small and larger grains. Thus the final spectrum may be expected to be a balance between small and large grains, set by the specific disk parameters.

In the *transitional disk* scenario, dust is cleared from the inner region and the forsterite is gradually mixed at larger radii. So basically these models show the effect of a decreasing average forsterite temperature. This scenario is limited in understanding the origin of the gap and the forsterite in the outer disk. E.g. it is yet not understood if the presence

of cold forsterite is due to in situ formation in the outer disk or is radially mixed outward. Figure 6.7 shows that if the forsterite is at larger radii in the disk, the I_{23}/I_{69} ratio decreases. Since the temperature is lower in the outer disk, the peak of the disk emission shifts towards longer wavelengths and the strength of the 69 μm feature increases in strength compared to that of the 23 μm feature. This may partly explain the forsterite spectra of transitional disks with known large gaps such as Oph IRS 48 and HD 141569.

An important insight follows from the *radial mixing* modeling grid for objects with strong forsterite features detected in the Spitzer/IRS spectrum, but no 69 μm feature detections. Figure 6.7 shows that if forsterite is only present in the inner disk, the 69 μm feature is much weaker than the 23 μm feature. There are two reasons for this effect. The first is based on the temperature. Even if the forsterite is hot, the 69 μm feature may not be visible in the spectrum because continuum emission from colder regions of the disk (where no forsterite is present) dominates. The second effect is that the integrated strength of the 69 μm band is three times weaker for 295 K compared to 50 K forsterite (see Section 6.3.1). In addition, because the feature gets broader towards higher temperatures, the peak flux of the 69 μm feature decreases almost an order of magnitude (see Figure 6.6). It is thus expected that the 69 μm feature will further broaden and decrease in strength for temperatures above 295 K. The low upper limits of the 69 μm detections typically show very large values of $I_{23}/I_{69} \sim 100$ (most notably for Group II sources). Since a forsterite abundance of 10 % between 0–5 AU gives a $I_{23}/I_{69} = 15.2$, this suggests that forsterite must be even closer to the star ($\sim 1-2$ AU). Because forsterite only resides in these hot inner regions of the disk, radial mixing is likely not an efficient process.

We find that within a limited mass range, *optical depth* effects can enhance the 69 μm feature as it becomes optically thin while the disk is still optically thick at 23 μm. This may explain the higher detection rate of the 69 μm feature for disks with a lower mm luminosity (Figures 6.3). There are three principal cases for the relative optical depth at 23 and 69 μm. The first situation is that the disk is optically thick at both 23 and 69 μm. This is the case for a disk mass of $M_{dust} = 3 \times 10^{-4}$ $M_{\odot}$. The optical depths scale relative to the density. So under the assumption that forsterite is vertically well mixed, the feature strength ratio is quite constant. The second situation is that the disk becomes optically thin at 69 μm while it is still optically thick at 23 μm ($M_{dust} = 3 \times 10^{-5}$ $M_{\odot}$). In this case, the 69 μm feature becomes stronger and the feature strength ratio decreases. Thirdly, the disk mass is so low that the disk is optically thin at both wavelengths. In this situation, all forsterite is visible to the observer and the feature strength ratio increases again.

Models predicting strong 69 μm features and weak features at shorter wavelengths are the grain growth scenario (where the emission is dominated by larger $\gtrsim 1$ μm forsterite dust), the transitional disk scenario (where only cold forsterite is left in the disk), and the optical depth scenario (the mass of small dust grains decreases and the disk becomes optically thin at 69 μm while it is still optically thick at 23 μm).

The opposite case where the 69 μm feature is weak compared to strong short wavelength forsterite bands can be explained due to inefficient radial mixing. In this scenario, forsterite is only present in the inner disk within a few AU. The location in the disk where the forsterite is hot depends on the stellar properties and geometry of the inner disk. For the

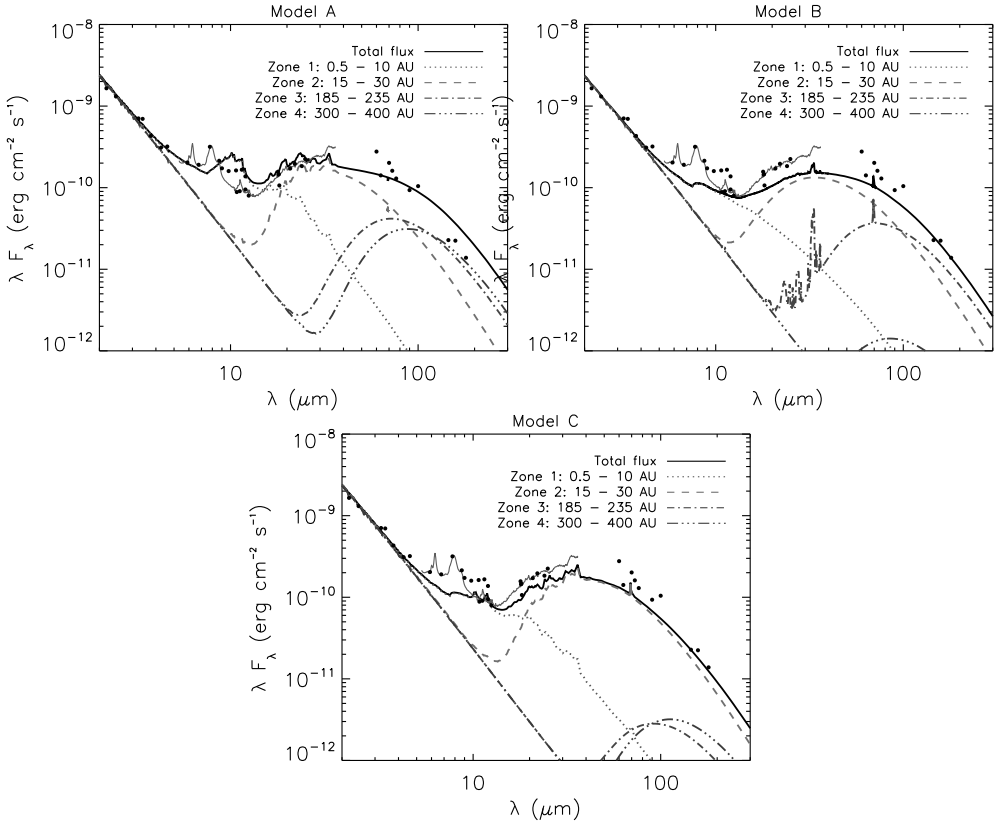

Figure 6.8: *SEDs of three models of HD141569. Top left: model A, small (1 μm) forsterite grains. Top right: model B, small (1 μm), cold, iron rich forsterite grains. Bottom: model C, large (10 μm) forsterite grains.*

continuous disk models presented in this section, the surface temperature of the disk is $\gtrsim$ 200 K at radii $\lesssim$ 3 AU. If the grains in the disk are mixed outward, then the 69 μm feature rapidly increases in strength. A mixing of 10 % forsterite in the inner 5 AU would result in a I_{23}/I_{69} ratio of 15.2. Since flat disks have an order of magnitude higher I_{23}/I_{69} ratios (Figure 6.4), we conclude that mixing is not efficient in flat disks.

6.5 The strong and broad 69 micron band of HD141569

In this section, detailed radiative transfer models of HD141569 are presented. HD141569 is selected for a case-study because we found in Section 6.2 that it is the most extreme outlier in the comparison between the forsterite temperature derived from the I_{23}/I_{69} feature strength ratio (T $\lesssim$ 70 K), and the temperature estimate obtained from the shape of the 69 μm feature (T $\sim$ 174 K).

6.5.1 Disk modeling approach

We focus on the dust mineralogy to constrain the size and location of forsterite. We first derive the geometry of the disk responsible for the dust continuum emission. Thereafter, we explore the properties of the grains that can fit the forsterite spectrum. We search for solutions which can reproduce the relative band strength I_{23}/I_{69}, the shape of the 69 μm feature and simultaneously fit the SED.

From earlier studies of the disk of HD141569, it is known that the disk of HD141569 is gas rich and is in the transition to a debris disk system (e.g. Augereau et al. 1999, Fisher et al. 2000, Clampin et al. 2003, Thi et al. 2014). Since we focus on the properties of the dust, our first step is to construct a geometrical model of the dust disk of HD 141569. We use the stellar properties derived in van den Ancker et al. (1998), with temperature $T_* = 9520$ K, luminosity $L_* = 18.3$ $L_\odot$ and distance $d = 99$ pc. The radiative transfer and dust model are described in Section 6.3. The modeling approach is largely similar to the benchmark model described in Section 6.4. The radial dependence of the surface density is parametrised by a power law with index -1. We assume a gas-to-dust ratio of 100. The dust size ranges from $a_{\rm min}$ up to $a_{\rm max}$ and follows a power-law distribution with $a_{\rm pow} = -3.5$. The maximum grain size $a_{\rm max}$ is set at 1 mm. The minimum grain size of the amorphous dust, as wel as the forsterite grains, is determined through simultaneously fitting of the forsterite features and the SED. The disk mass is also derived by fitting of the SED. We assume an amorphous dust composition of 80% silicate and 20% carbon for the dust emitting the continuum emission. Forsterite of either 1 or 10 μm size grains is mixed in the disk at certain radii in order to fit the forsterite spectrum.

6.5.2 The geometry of the disk

We construct a disk model that is based on available imaging data and the SED. In order to successfully fit the continuum emission of the SED, we find that it is required to break up the disk into four zones, with the following characteristics. Zone 1, between $0.5-10$ AU, is the innermost disk and is derived by a fit to the SED between $\sim 5-12$ μm. Therefore, zone 1 has a typical dust temperature between $\sim 150-1000$ K. Note that the continuum emission between the PAH features does not originate from the PAHs (Maaskant et al., 2013). We do not fit the PAH features in this model. Disk zone 2, between $15-30$ AU, accounts for the MIR emission bump between ~ 12 μm up to at least ~ 100 μm. The presence of this disk zone is inferred due to the bump in the SED, which is indicative of a high vertical disk wall that produces a strong single temperature emission component at ∼100 K. MIR imaging observations by Fisher et al. (2000) are consistent with the presence of such a disk zone, since quadratic deconvolution of the source with the PSF gives FWHM sizes of 34 AU at 10 μm and 62 AU at 18 μm for the extended emission near the star. However, we do not model the MIR observations, so we cannot accurately determine the inner and outer location of disk zone 2. Therefore we arbitrarily set zone 2 between $15-30$ AU, which results in typical dust temperatures between $\sim 70-100$ K. The presence of disk zone 3 and zone 4, located between respectively $185-235$ AU and $300-400$ AU, are inferred from direct scattered light observations (Augereau et al.,

1999, Clampin et al., 2003). From our model, we derive typical temperatures in zone 3 and 4 of $\sim$ 40 K and $\sim$30 K respectively.

Figure 6.8 shows three SEDs of forsterite models which we present in the next section. A degeneracy which follows from the SED fit is whether the outermost zones 3 and 4 dominate the continuum at long wavelengths. The observed photometry can be fitted by the Rayleigh Jeans tails of disk zones 2, 3 and 4 as shown in Figure 6.8. Millimetre imaging is needed to lift this degeneracy.

6.5.3 Fitting the forsterite

We want to reproduce the low forsterite I_{23}/I_{69} band strength ratio as well as the shape (i.e. the width and peak position) of the 69 μm feature. We do not aim to derive a perfect fit. Instead, we identify the most important parameters that play a role in fitting the forsterite spectrum. Referring back to the parameter study presented in the previous section, we can already indicate in what regions of the parameter space we can find solutions. In general, a low I_{23}/I_{69} ratio can be explained by cold forsterite (as in the transitional disk scenario), or larger grains. Optical depth effects do not play a role because we find in our models that because of the low mm luminosity, the disk mass is also very low and therefore the disk is optically thin.

To be consistent with the shape of the forsterite 69 μm feature, we need to include an effect that broadens the band while the forsterite is cold (i.e. to ensure a low I_{23}/I_{69} ratio). There are two effects that can produce that result. The first solution is by including an iron distribution. This has been done in detail by Sturm et al. (2013), who find that an iron fraction between 0–1.2 % (derived by interpolation between laboratory measurements between 0–8 %) of forsterite can fit the 69 μm feature of HD 141569. The second solution is by including forsterite grain size larger than a few micron (Section 6.4.2).

There are only two locations in the disk from which forsterite emission can observed the spectrum. From disk zone 2, which dominate the SED at MIR wavelengths, and from disk zone 3, which has a smaller contribution to the SED because the dust is colder. Forsterite emission from disk zones 1 and 4 is respectively too hot and cold to be observed.

In the next sections we present three forsterite models. Model A shows that 1 μm forsterite grains in disk zone 2 do not fit the observed spectra. Then we present two different models which do give a fit to the spectrum. Model B, with very cold, 1 μm, iron containing, forsterite in disk zone 3, and Model C, with forsterite grains of 10 μm mixed in disk zone 2. The parameters of the three models that are used to fit the forsterite spectrum, as well as the SED, are shown in Table 6.4. Spectra and sketches of these models are shown in Figure 6.9. In the discussion (Section 6.6.3) we evaluate the model solutions, discuss which formation histories are required for both scenarios, and argue that model C, using larger 10 μm grains, is favoured.

Table 6.4: *Characteristics of three HD 141569 models.*

Parameter	Unit	Model A	Model B	Model C
Disk total dust mass	$M_\odot$	3.1×10^{-6}	1.2×10^{-6}	9.5×10^{-6}
Disk zone 1				
Disk location	AU	0.5 – 10	0.5 – 10	0.5 – 10
Disk, dust mass	$M_\odot$	5×10^{-10}	7×10^{-10}	7×10^{-10}
Forsterite fraction	...	0	0	0
Min. dust size	μm	1	10	10
Disk zone 2				
Disk location	AU	15 – 30	15 – 30	15 – 30
Disk, dust mass	$M_\odot$	1×10^{-7}	1×10^{-7}	5×10^{-7}
Forsterite fraction	...	0.07	0	0.07
Min. dust size	μm	1	10	10
Disk zone 3				
Disk location	AU	185 – 235	185 – 235	185 – 235
Disk, dust mass	$M_\odot$	1×10^{-6}	1×10^{-6}	3.0×10^{-6}
Forsterite fraction	...	0	0.2	0
Min. dust size	μm	1	1	10
Disk zone 4				
Disk location	AU	300 – 400	300 – 400	300 – 400
Disk, dust mass	$M_\odot$	2×10^{-6}	1×10^{-7}	6.0×10^{-6}
Forsterite fraction	...	0	0	0
Min. dust size	μm	1	1	10

6.5.3.1 Model A: small forsterite grains

Model A incorporates (iron-free) 1 μm forsterite grains in disk zone 2. A mass abundance of 7% forsterite in zone 2 of the disk was needed to fit the peak flux of the 69 μm flux. This model gives several problems. As Figure 6.9 shows, the forsterite features at short wavelengths are over-predicted and the shape of the 69 μm band does not match the observation because the forsterite is too warm. The peak position of the 69 μm feature is too blue and the width is too narrow. As the peak position is sensitive to the iron content of forsterite, this could be alleviated by including a distribution of iron (Section 6.5.3.2).

The upper plot of Figure 6.8 shows that the SED of the disk is not well fitted. Because we assume that the minimum size of the amorphous silicate dust grains are equal to the forsterite grains, the 10 μm amorphous silicate features shows up in the spectrum. This feature originates from zone 1, thus we find that the innermost disk zone 1 is depleted of small ($\lesssim$1 μm) dust grains. Second, if the outermost zones 3 and 4 contribute $\sim$50 % of the emission at 69 μm, the SED at mm wavelengths is over predicted. Thus, we learn that

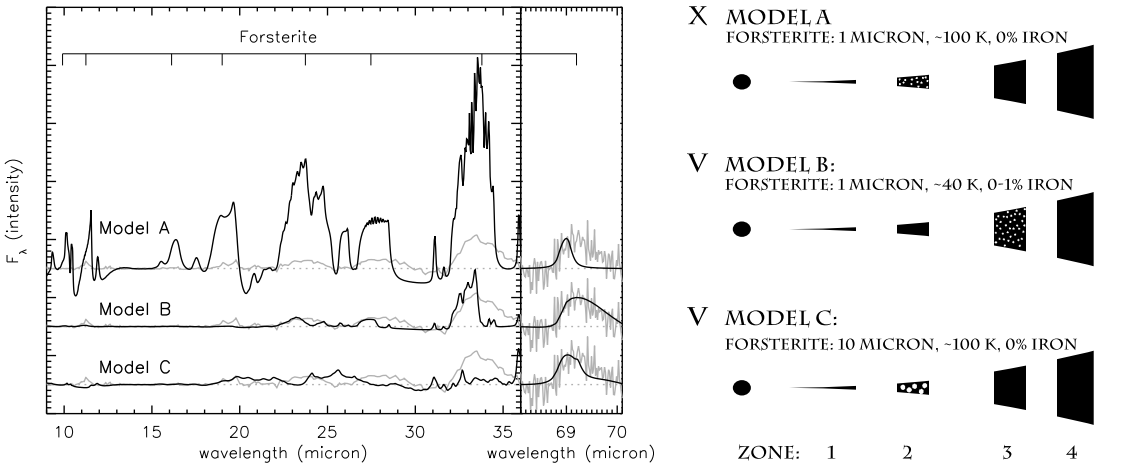

Figure 6.9: *The forsterite spectra of model A, B and C to HD141569. The black line is the model and the grey line is the data. Model A fails to fit the data, while model B and C give reasonable good fits. See text for model details. The right panel gives schematic representations of the disk structures. Four disk zones are needed to fit the SED and direct imaging observations. The 'X' symbol means that the model fails to fit the spectrum, the 'V' symbols shows the best fitting models.*

disk zone 2 dominates the continuum emission in the MIR and FIR from $\sim$ 14 μm up to at least $\sim$100 μm, and that the contribution from disk zones 3 and 4 at these wavelengths is small.

The assumption of thermal contact between the forsterite grains and the other disk components has consequences for the emission spectrum of forsterite. For this model, we have tested the scenario where the forsterite is not in thermal contact with the amorphous dust. We find that the temperature and more noticeably, the luminosity of forsterite decreases. Nevertheless, after scaling the abundance up to fit the 69 μm feature again, the forsterite is still too warm (i.e. the short wavelength features are still over-predicted).

6.5.3.2 Model B: small, cold, iron rich forsterite grains

In model B, 1 μm forsterite grains are mixed in zone 3, where they are further away from the star and thus colder. In order to fit the 69 μm feature, an abundance of 20 % forsterite in zone 3 is needed to fit the strength of the 69 μm feature. Because of the lower temperature in zone 3, the short wavelength features are much weaker. To prevent the model from producing the amorphous 10 and 20 μm silicate features, the minimum grain sizes in the innermost zones 1 and 2 are set at 10 μm. Note that this model implies that there is no contribution from warmer crystalline silicate grains in zone 2.

The shape of the 69 μm feature is fitted by assuming that the forsterite has a Gaussian distribution of different iron fractions. It has been shown by laboratory measurements that already an iron fraction of 8 % shifts the position of the 69 μm feature from 69 to 72 μm (Koike et al., 2003). Since iron increases the peak wavelength to the red, a Gaussian

distribution between 0 and 1 % iron can broaden the feature significantly. In Figure 6.9 it is shown that a distribution of iron fractions between $0-1$ % fits the feature well. The shape of the 69 μm has been calculated using weighted interpolations of different iron fractions. The method of interpolation is described in de Vries et al. (2012).

6.5.3.3 Model C: large forsterite grains

Model C presents a solution using iron-free forsterite grains of 10 μm in disk zone 2, using a mass abundance of 7% to fit the strength of the 69 μm feature. Similar to the grain size of the forsterite, the minimum grain size of the amorphous dust in the innermost zone 1 and 2 are set at 10 μm. For consistency, the minimum grain size in disk zones 3 and 4 are also set at 10 μm. The increased grain size influences the opacity profile of forsterite (see Figure 6.6). The shorter wavelength features are much weaker and the width of the 69 μm feature is naturally fitted, though the peak position of the model is slightly too blue (~ 0.2 μm) compared to the observed feature. Because the features between $25-35$ μm seem to change in position, the points where the continuum is subtracted for this model is changed from 21.75 and 26.4 μm to 23.5 and 29 μm.

6.5.4 Summary of HD 141569 modeling

Two models reasonably fit the observed spectrum of HD 141569, model B using respectively iron rich, ~ 40 K, 1 μm forsterite in zone 3, and model C, using iron free ~ 100 K, 10 μm forsterite in zone 2. Note that any model combining the parameter sets of these two cases would likely also fit the observations. For example, the short wavelengths forsterite features are not well fitted in model C, but this issue may be resolved by adding a small amount of small 1 μm forsterite grains (while the 69 μm feature is still dominated by the larger ~ 10 μm forsterite grains). Forsterite formation scenarios will have to explain how forsterite can be present at large distances from the central star and why they are either iron rich, or depleted of small grains. In Section 6.6.3 we will discuss both scenarios.

6.6 Discussion

The composition and sizes of forsterite grains are results of physical processes that take place during the evolution of protoplanetary disks. In the inner regions of disks where temperatures are high ($\gtrsim 1000$ K), forsterite can be formed through gas phase condensation and/or thermal annealing. The crystals may then be transported to the cooler outer parts of the disk. Scenarios include radial mixing in the disk (e.g., Bockelée-Morvan et al. 2002, Gail 2004, Davoisne et al. 2006, Jacquet 2014) and disk winds (e.g. Shu et al. 1994). Alternatively, crystalline silicates can be formed in-situ in the outer disk by shock waves (Harker & Desch, 2002, Desch et al., 2005), lightning (e.g. Pilipp et al. 1998), parent body collisions (Urey, 1967, Huss et al., 2001, Morlok et al., 2010), and stellar outbursts

(Juhász et al., 2012). To understand the significance of these scenarios, it is important to characterize the location, composition and sizes of forsterite grains in protoplanetary disks.

6.6.1 Forsterite in flat disks

We find that the I_{23}/I_{69} ratios of flat disks in our sample indicate high ($\gtrsim$ 200 K) forsterite temperatures. Since such temperatures are only found in the inner $\lesssim$ 5 AU of a continuous disk (i.e. no gaps), this shows that forsterite emission predominantly originates from the inner region in flat disks. Hence, the observations suggest that for flat disks, forsterite formation occurs in the hot inner region of the disk.

We find by radiative transfer models in Section 6.4 that the 69 μm feature is weakest if forsterite is only present in the inner few AU of the disk. If forsterite becomes abundant in colder regions of the disk, than the 69 μm feature rapidly increases in strength and should have been detectable. As the radial size of the T $\gtrsim$ 1000 K zone, where forsterite can form by annealing or vapor condensation, is small, the presence of forsterite features at short wavelengths imply that forsterite have diffused outward somewhat. However, the absence of the 69 μm features indicates that the diffusion process does not efficiently transport forsterite grains to the outer disk further than ∼5 AU.

The presence of (weak) 69 μm features in HD 104237 and HD 144668 and their absence in the other flat disks, may reflect optical depth effects. Among all flat disks, HD 104237 and HD 144668 have the lowest mm brightness and have the lowest I_{23}/I_{69} (besides HD 144432, but this is an upper limit). Since mm emission is optically thin, the low mm luminosities may imply lower disk masses. When the disk mass is lower, the disk is also more optically thin. In that case, the region where the forsterite is located may become optically thin at 69 μm while it is still optically thick at MIR wavelengths. Alternatively, forsterite grains may have been diffused outward to colder regions of the disk, or may have grown to larger sizes. All of these effects enhance the strength of the 69 μm feature and lower the I_{23}/I_{69} ratio. Although we cannot determine which evolutionary model is favourable, they all suggest that the detection of the 69 μm feature in flat disks is connected with disk evolution.

6.6.2 Forsterite in transitional disks

Many, if not all Herbig disks with disk classification group I are disks with large gaps and can be characterized as (pre-)transitional. An evolutionary path from the observed group I to the observed group II sources seems no longer likely. Instead, both might derive from a common ancestor, or group I objects may originate from group II sources (Maaskant et al., 2013). The variety in the results of our study for transitional disks (group I sources) is puzzling, in particular in connection with the fact that cold forsterite appears to be absent in flat disks (group II sources). For the transitional disks, we find that the majority of these disks do not have a detectable amount of cold forsterite (measured by

the presence or absence of the 69 μm feature). However, for a few sources, significant amounts of forsterite are present in the cold outer regions. The high crystalline mass fraction in the inner edge of the outer disk of HD 100546 (Mulders et al., 2011) seems to indicate that the cold forsterite is connected to the formation of the gap. As suggested by Bouwman et al. (2003), forsterite grains may be blown outwards on the wall by radiation pressure. However, this scenario would not work efficiently if significant amounts of gas resides in the gaps (as is the case for the transitional disks of Oph IRS 48, HD 141569 and HD 100546, Bruderer et al. 2014, Thi et al. 2014, Acke & van den Ancker 2006. Also for HD 100546, the non-negligible accretion rate derived by Deleuil et al. (2004) argues against outward radial mixing through the gap.

A possibility to explain the cold forsterite would be that the mixing in an earlier evolutionary state is more efficient than we derive, and that the forsterite is hidden in the disk and only exposed and made visible when the gap opens and the disk rim is illuminated. Perhaps the forsterite grains hide in the midplane after growing and settling and become visible when the disk mass decreases due to optical depth effects. Another option is that the forsterite is locally produced in the transitional disks where it is observed. This would also suggest a connection to the gap forming process, but is clearly not a process that is always linked to the formation of gaps.

When looking at this result in the terms of an evolutionary picture, the following scenarios and questions arise. If we assume that transitional disks are the evolutionary successor to flat disks, then we would in the first instance not expect significant amount of forsterite in the outer disk. Since radial mixing does not appear to be effective in flat disks, the situation just before the opening of a big gap would be that little or no forsterite present at low temperatures in the outer disk. Direct radial mixing would become infeasible in a disk with a large gap. If, however, the transitional disks and flat disks have evolved from a common ancestor, but represent different paths of disk evolution, than the large dispersion in abundances of cold forsterite in transitional disks still remains to be explained in this framework.

6.6.3 Larger grains in group Ib transitional disks

HD 141569 and Oph IRS 48 are transitional disk which lack the 10 and 20 μm amorphous silicate features, but instead show prominent PAH emission bands in their spectra. This is an indicator of large gaps which have depleted the population of small ($\lesssim 1$ μm) dust grains in the temperature region of the disk where amorphous silicate features are produced (Maaskant et al., 2013). The 69 μm features of HD141569 and Oph IRS 48 are remarkably strong and have large widths indicating temperatures of $\sim 150-200$ K. This is however not consistent with the temperature derived from the I_{23}/I_{69} ratio ($\sim 50-100$ K). We have found by detailed modeling of HD 141569 that there are two scenarios that fit the forsterite spectra. In the first scenario (model B), the forsterite is located in the outer disks at ~ 200 AU where temperatures are below $\lesssim 40$ K, an iron distribution has been used to fit the width of the 69μm feature. In the second scenario (model C), the forsterite is modelled by larger (10 μm) grains in the disk zone which also produces the mid- to

far-infrared continuum emission. The larger grain size broadens the 69 μm feature and decreases the strength of the features at lower wavelength. Combinations of these two extreme models may also fit the spectra.

We now discuss the forsterite formation histories required to explain both model solutions. For model B, it is difficult to understand that there is a mass abundances of ∼20 % in the disk at ∼ 200 AU, while no forsterite grains are present in the innermost disk zones. If shock heating, parent body collisions or radial mixing are responsible for the cold forsterite, we may expect this to be more efficient closer to the star due to higher densities and relative velocities. Also the Gaussian distribution of iron fractions between $0-1$ % has no clear origin. The shape of the 69 μm feature of HD 141569 is comparable to that of Oph IRS 48. The inner edge of the outer disk of Oph IRS 48 has a temperature ∼120 K and is located at ∼60 AU (Maaskant et al., 2013). However, there is yet no observational evidence of a large colder ($T \lesssim 50$ K) outer disk at $\gtrsim 200$ AU for Oph IRS 48. A model with a dominant contribution of cold, iron rich forsterite (model B) seems much more difficult to construct for Oph IRS 48. Model C, the scenario with a dominant contribution of larger (i.e. 10 μm) grains, does not have these difficulties. In addition, our solution of larger forsterite grains in the disks of HD 141569 and Oph IRS 48 seems to be consistent with significant depletion of small grains in group Ib sources. For all these reasons, we consider model C to be a more likely scenario to explain the forsterite spectrum of HD 141569 and Oph IRS 48. In this scenario, the larger width of the forsterite 69 μm feature can be used as an independent indicator of larger grains sizes in protoplanetary disks.

6.7 Conclusions

We have performed a detailed radiative transfer study to examine the observational behaviour of forsterite spectra under several evolutionary scenarios. In particular we check for consistency between the forsterite I_{23}/I_{69} feature strength ratio, and the shape of the 69μm feature and study HD 141569 in detail as it is the most extreme outlier in the sample. Our findings are:

- Forsterite in flat (group II) disks is located in the inner few AU. This indicates that radial mixing is an inefficient process, at least in flat disks, or that local production does not take place.
- The detection rate of the 69 μm forsterite feature is higher for objects with lower millimeter luminosity. This may indicate that as disks evolve toward lower masses, optical depth effects or increased production/transportation of forsterite in/to cold regions of the outer disk enhance the strength of the 69 μm feature.
- The I_{23}/I_{69} ratio is an independent forsterite temperature indicator, and is most inconsistent with the observed 69 μm shapes of HD 141569 and Oph IRS 48.

- The large widths of the 69 μm features of HD 141569 and Oph IRS 48 can be explained by forsterite grains with sizes above a few micron, or by a distribution of iron fractions between $\sim 0-1$ %.
- The weak 23 μm feature compared to the 69 μm band strength in the evolved transitional objects HD 141569 and IRS 48 can be explained by very cold, or larger grains.
- The innermost disk of HD 141569, responsible for the continuum emission between $\sim 4-14$ μm, does not contain small ($\lesssim 1$ μm) amorphous and crystalline silicate grains.
- Radiative transfer models show two solutions to fit the larger width of the forsterite 69 μm band, consistently with the low I_{23}/I_{69} feature strength ratio of HD 141569. A model with iron rich ($\sim 0-1$ % Fe fraction), ∼40 K, 1 μm grains (model B) and a model using iron free, ∼100 K, 10 μm grains (model C). We argue that the model with larger ($\gtrsim 10$ μm) forsterite seems to be most likely.

Acknowledgements: *The authors thank the anonymous referee for his/her excellent comments and constructive feedback. The authors thank Neal Evans, Gwendolyn Meeus, Thomas Henning, Jeroen Bouwman, and the members of the Herschel DIGIT team for useful discussions which improved the analysis presented in this paper. The authors thank Gijs Mulders and Inga Kamp for useful comments on the manuscript. K.M. is supported by a grant from the Netherlands Research School for Astronomy (NOVA). M.M. acknowledges funding from the EU FP7-2011 under Grant Agreement No 284405. Studies of interstellar chemistry at Leiden Observatory are supported through advanced-ERC grant 246976 from the European Research Council, through a grant by the Dutch Science Agency, NWO, as part of the Dutch Astrochemistry Network, and through the Spinoza premie from the Dutch Science Agency, NWO.*